Process Simulation - Current Status and Future Needs

W. Fichtner

AT&T Bell Laboratories
Murray Hill, NJ 07974

ABSTRACT

New developments and results in the area of process simulation are reviewed. These results have increased significantly our understanding of the underlying processes that govern integrated circuit (IC) fabrication techniques.

I. Introduction

With the increasing demand for larger circuit complexities, the process steps necessary to fabricate chips have become very complicated. In order to keep the die area constant (1 cm^2), the staggering increase in complexity has been achieved mainly by scaling the vertical and lateral dimensions of the various building blocks of the integrated circuit (IC).

The use of computer programs to aid process engineers in the development of new semiconductor technologies has become a worthwhile alternative to the conventional *trial-and-error* experiments. The results of computer programs, if properly used and analyzed, can have a significant impact on the design optimization cycle by drastically reducing the time needed to develop a process [1].

Modern processes allow the classification of IC fabrication steps into three areas: 1) Thermal processing and doping; 2) pattern definition (lithography); and 3) pattern transfer (etching and deposition). Table I summarizes the various process steps that fall into these categories.

This paper was written as an update to an earlier tutorial on process simulation [2] in order to focus on recent developments in this field. It is interesting to follow the development of process simulation during the past few years [e.g.3]. This rather new field of applied computer modeling is a typical example of an *demand-driven* discipline which is constantly refined to keep up with current developments in technology. Compared to device simulation, process modeling lags behind several years. While device simulation programs have reached a level of sophistication which allows even prediction with a high probability of success, process simulation often relies on empirical simplifications to model a certain problem. Device physics is a established field. A large amount of knowledge has been accumulated since the invention of the transistor. Today, we know in detail the basic equations, mechanisms and phenomena governing current transport in silicon devices. The situation is completely different for process simulation. For most of the process steps in Table I, our knowledge of the underlying physical and chemical processes is still unsufficient to attempt first principles solutions.

For this paper, I have chosen to concentrate on three different areas with new developments during the past three years.

(1) Ion Implantation

Ion implantation is the main workhorse of the semiconductor industry. It is used to selectively dope active areas with a controlled amount of doping. In section II, I shall present some new results on implantation modeling and profile construction.

(2) Oxidation-related Phenomena

The understanding of the atomic processes governing diffusion of substitutional impurities (As, B, P, and Sb) has increased considerably. Section III will focus on recent results on oxidation-related diffusion phenomena.

(3) Optical Lithography

Optical lithography has traditionally dominated the pattern definition field, and it will certainly continue to do so till we have reached feature sizes of 0.5μm. The methods used for pattern definition have evolved over the past fifteen years form optical contact printing of negative resists via a transition phase with 1:1 projection printing to direct step on wafer (DSW) (10:1 or 5:1) projection printing. In section IV, I shall summarize the basic theory of optical projection printing.

Section 5 contains a discussion of the future of process simulation.

II. Ion Implantation

The successful fabrication of scaled devices depends strongly on the ability to predict as-implanted profile distributions as well as the associated electrical and mechanical effects for given conditions.

A classification of all important theories and calculational procedures is shown in Table 2 [4], which also summarizes major developments in the field. The pioneering work of Lindhard and coworkers [19-21] on the transport equation formalism has been refined by many authors. To my knowledge, all published range distributions have been derived from the original LSS approach. However, all these methods have the severe restriction that they require the assumption of a homogeneous target. Therefore they are no applicable to simulate multilayered targets. Furthermore, these methods cannot be extended in a straightforward manner to simulate multi-dimensional problems.

1. Monte-Carlo Calculations and Ion Scattering

With the availability of high speed digital computers, ion transport calculations using the Monte-Carlo technique have become very popular. The program MARLOWE, developed by Oen and Robinson [22,23], treats the scattering process by exactly evaluating the scattering integral for the scattering angle in the center-of-mass (CM) system

$$\Theta = \pi - 2\,p \int_{r_0}^{\infty} \frac{dr}{r^2\,[r - \frac{V(r)}{E_r} - \frac{p^2}{r^2}]^{\frac{1}{2}}} \qquad (1)$$

where p is the impact parameter, $V(r)$ is the interaction potential between the incident ion (mass M_1, charge Z_1) and the target ions (mass M_2, charge Z_2), r_0 is the

distance of closest approach, and $E_r = E/(1+M_2/M_1)$ is the energy in the CM-system.

MARLOWE is capable of simulating arbitrary structures (amorphous, polycrystalline and crystalline). From my experience, I can highly recommend this excellent code, whose only drawback lies in the required computing resources.

For process simulation purposes, a variety of different models have been developed: i) the local structure model [17], ii) the dense gas model [24], and iii) the liquid structure model [25]. The major differences between these approaches lie in the treatment of nuclear scattering, the representation of the target structure and the formulation of the mean free path.

Using the local structure model, Biersack and Haggmark have developed the program TRIM, which has been refined by Macrander [18] and adapted to a vector processor by Petersen et al. [26]. Miyagawa and Miyagawa [25] and Adesida and Karapiperis [27] have developed the programs SASAMAL and PIBER based on the liquid model.

The difference between TRIM and the other codes lies in the treatment of nuclear collision. In TRIM, the impact parameter p is determined from a random number $0 \leqslant R_n \leqslant 1$, and the angle Θ is calculated from

$$\left(\frac{p}{r_0}\right) - \frac{V(r_0)}{E_r} - 1 = 0 \qquad (2)$$

where $V(r)$ is the Moliere from of the Thomas-Fermi potential

$$V(r) = \frac{Z_1 Z_2}{r} \phi\left(\frac{r}{a}\right) \qquad (3)$$

with the screening radius a, and

$$\phi(x) = 0.35\exp(-0.3x) + 0.55\exp(-1.2x) + 0.1\exp(-6x) \qquad (4)$$

The energy tranfer T to the target atom in a single collision is determined by

$$T = \frac{4M_1M_2}{(M_1 + M_2)^2} E \sin^2\frac{\theta}{2} \qquad (5)$$

In the dense gas and the liquid model, T is calculated from the differential nuclear cross section

$$d\sigma(E,T) = \pi a^2 \frac{dt}{2t^{\frac{3}{2}}} f(t^{\frac{1}{2}}) \qquad (6)$$

which depends only on a single parameter t

$$t^{\frac{1}{2}} = \epsilon \sin\frac{\theta}{2} \qquad (7)$$

where ϵ is the reduced energy

$$\epsilon = \epsilon_1 E = \frac{M_2}{M_1 + M_2} \frac{a}{Z_1 Z_2 q^2} E \qquad (8)$$

with the electric charge q. The universal scattering function $f(t^{\frac{1}{2}})$ depends on the form of the potential $V(r)$ in Eq. (3). It can be represented by

$$f(t^{\frac{1}{2}}) = \lambda \frac{t^{\frac{1}{2}-m}}{[1 + (2\lambda t^{1-m})^q]^{\frac{1}{q}}} \tag{9}$$

Several authors have published values for the fitting parameters in the above equation.

Figure 1 compares mean projected ranges R_p and standard deviations ΔR_p for ^{11}B implanted into silicon over a wide range of energy. The B–Si ion-target combination is a severe test for any code due the small mass ratio M_1/M_2. Both TRIM and SASAMAL (with two different cross-sections) fit the experimental data very well. The analytical results are data obtained from the tables published by Gibbons et al. [28] and Brice [29].

For mass ratios $M_1/M_2 > 1$, nuclear stopping completely dominates the slowing down process. Miyagawa and Miyagawa [25] have compared range data for ^{122}Sb with various computer programs (Fig. 2). Best agreement is obtained for SASAMAL with the Kalbitzer-Oetzmann [32] cross section. All other calculations underestimate the range by 20%. This result is not surprising, since the experimental data were the origin of the improved fitting to the parameters of the f-function.

Monte-Carlo calculations have been particularly successful in the calculation of multi-dimensional ion distributions. Mazzone and Rocca [34] have recently published results on ^{31}P implantations into amorphous and crystalline silicon. They have extended the original treatment by de Salvo and Rosa [35] to allow simulations for arbitrarily shaped targets.

Figure 3 shows ion distributions in the vicinity of a $Si-SiO_2$ step obtained for an amorphous silicon substrate. Each dot presents the final coordinate of a number of ions in a pixel. The more interesting case occurs in the case of a crystalline silicon substrate. Figure 4 should be compared with Fig. 3. The incidence conditions are the same for both results, and in both cases the beam is tilted 7.5° off the <100> axis. The results in Fig. 4 represent the situation for a low dose implant which leaves the lattice undisturbed.

Boltzmann Transport Equation

Ion implantation can be visualized as a transport problem with the motion of ions during their slowing-down to zero energy. A collection of particles with velocity $\mathbf{v}$ at coordinated $\mathbf{x}$ can be described by the distribution function $F(\mathbf{v},\mathbf{x})$

$$dN = F(\mathbf{v},\mathbf{x}) d^3\mathbf{v}\, d^3\mathbf{x} \tag{10}$$

and the probability for a particle with velocity $\mathbf{v}$ to scatter into the velocity element $[\mathbf{v}',\mathbf{v}' + d^3\mathbf{v}]$ during the time dt is given by

$$K(\mathbf{v}\rightarrow\mathbf{v}')\, d^3\mathbf{v}'\, dt = N_s |\mathbf{v}|\, d\sigma(\mathbf{v}\rightarrow\mathbf{v}') dt \tag{11}$$

where $K(\mathbf{v}\rightarrow\mathbf{v}')$ is the transition rate, N_s is the density of scattering centers and $d\sigma$ is the differential cross section. The average number of ions scattered into a differential phase space element is described by a Boltzmann Transport Equation for the distribution function

$$\frac{\partial F(\mathbf{v},\mathbf{x})}{\partial t} + \mathbf{v}.\nabla F(\mathbf{v},\mathbf{x}) = N_s \int \left[d\sigma(\mathbf{v}'\rightarrow\mathbf{v})\, |\mathbf{v}'|\, F(\mathbf{v}',\mathbf{x}') - d\sigma(\mathbf{v}\rightarrow\mathbf{v}') |\mathbf{v}|\, F(\mathbf{v},\mathbf{x}) \right] + Q(\mathbf{v},\mathbf{x})\ . \tag{12}$$

The quantity Q is a generation term which allows particles to be created from rest.

This accounts for recoils generated by primary particles. If more than one projectile type is involved, subscripts should be added in Eq. (12).

Integration of this equation is carried out starting from $z=0$ (the sample surface) and integrated for $z>0$ with the initial condition

$$F(\mathbf{v},0) = N_D\, \delta(\mathbf{v}-\mathbf{v}_0) \tag{13}$$

where N_D is the total dose and $\mathbf{v}_0$ is the the initial velocity of the incident beam.

The integration of Eq. (12) requires that the motion of each particle in the distribution is confined to a finite number of discrete states.

Each state is defined by an energy E_i ($0 \leqslant E_i \leqslant E_o$) and an angle θ_j. In the work of Christel, Gibbons, and Mylroie [11,12], θ_j has been limited to a range between 0 and $\pi/2$. This restriction removes backscattered particles from the final distribution, and it fails in the case of very light projectiles impinging on heavy targets ($M_1/M_2 << 1$). To keep computation times reasonable, 150 discrete elements (15 equally spaced energy states and 10 angular intervals) were used. The step size Δz was set to 1Å. Giles and Gibbons [13] have developed a multipass algorithm where the region of interest is scanned iteratively until all particles have come to rest. At the end of the first pass, they obtain a concentration profile together with a set of matrices of backscattered ions. The second pass, however, is made from the target interior towards the surface, thus accounting for the motion of all ions backscattered in the original pass. Adding the stored backscatter distribution to the original profile, one proceeds until all ions have stopped. For multilayered targets, BTE calculations have been very successful in the simulation of recoil effects. Giles and Gibbons [13] have modelled a low-energy ^{11}B-implant (E = 15keV) through a 100Å layer of Au into Si. Figure 5 presents ^{11}B profiles in the Au-Si target as obtained by the multipass algorithm. While about 20% of the original dose are lost due to ^{11}B backscattering in the Au layer, the dose in the Si is slightly increased from 71% to 75% due to ^{11}B ions that were initially backscattered in the silicon and then returned due to backscattering at the Au-Si interface.

Pearson Distributions

The Pearson system of univariate distributions [36] can be classified as solutions to the equation

$$(b_0+b_1x+b_2x^2)\,\frac{df}{dx} = (x-a)f \tag{14}$$

where $f(x)$ is the frequency function and $x = z-\bar{z}$ is the distance from the mean $\bar{z}$. The coefficients b_i, $i=0,1,2$, can be expressed in terms of the moments $\mu_k = <x_k> = \int x^k f dx$, $k=1,\ldots,4$. The four constants a,b_i can be represented by the first four moments

$$a = \frac{-\gamma_1 \Delta R_p (\beta_2+3)}{A} \quad (15)$$

$$b_o = \frac{-(\Delta R_p)^2 (4\beta_2 - 3\gamma_1^2)}{A} \quad (16)$$

$$b_1 = a$$

$$b_2 = \frac{-(2\beta_2 - 3\gamma_1^2 - \Delta R_p)}{A} \quad (17)$$

$$A = 10\beta_2 - 12\gamma_1^2 - 18 \quad (18)$$

Different distributions are classified according to the behavior of the roots of

$$b_0 + b_1 x + b_2 x^2 = 0 \quad (19)$$

In Table III, $f(x)$ is the solution to Eq. (14) and k is a normalization factor imposed by the requirement that

$$\int_{a_0}^{a_1} f(x)dx = 1 \quad (20)$$

where

$a_0 = \max(0, x_-)$, $a_1 = x_+$ (Type I)
$a_0 = 0$, $a_1 = x_+$ (Type III)
$a_0 = 0$, $a_1 = \infty$ (Type IV)
$a_0 = 0$, $a_1 = x_-$ (Type VI)

This table also includes important conditions for various parameters (expressions in round brackets (. , . , .)) which have to be fulfilled to produce profiles with physical meaning.

Until recently, one-dimensional ion distribution profiles have been fitted by Pearson IV distributions. Winterbon [37] has reported that for high-energy implants, Pearson VI distributions seem preferable.

Petersen et al. have extended Winterbon's work by analyzing the As, B, P and Sb profiles obtained from Monte Carlo simulations [26]. Figure 6 is a plot of $\kappa = b_1^2/4b_0b_2$ as a function of energy for $^{11}B \rightarrow Si$. The parameter b_2 has a zero around $E = 100$ keV forcing a singularity in κ . For energy values below this singularity, the boron profile apparently is better fitted by a Type I Pearson distribution, while for large energy values it is better fitted by a Pearson VI distribution. These high energy data are equivalent to Winterbon's result [37] and strongly support his findings.

Corresponding results for ^{31}P, ^{75}As and ^{122}Sb are given in Fig. 7. For each element, the parameter κ is outside (0,1) and the roots of Eq. (19) are real. For all cases shown, a Type I distribution would be adequate to fit these ion ranges.

III. Oxidation-Related Diffusion Phenomena

In the recent past, new results on the effect of oxidation on the diffusion of substitutional dopants have greatly increased our understanding of the nature of point defects in silicon. Since impurity diffusion, together with ion implantation, is an integral process step of any modern technology, these results will have an important impact on the next generation of process simulators.

In analogy to metals, it was believed for a very long time that vacancies are the only point defect species in thermal equilibrium. To my knowledge, all important process simulators (SUPREM [38], BICEPS [39], ICECREM [40] etc.) incorporate diffusion models built on the vacancy model, originally developed by Fair[41]. A straightforward application of this model, however, cannot explain several important experimental facts, such as the high concentration diffusion of phosphorus, the diffusion behavior of all common dopants in Si in the presence of oxygen, and corresponding nitridation experiments.

Coexistence of vacancies (V) with silicon self-interstitials (I) was suggested by Seeger and Chick[42] and Hu[43]. The difficulties involved in finding the real nature of the dominant point defect in Si can be understood by looking at the silicon self-diffusion coefficient [44]

$$D^{SD} = 1460 \exp\left(\frac{-5.02}{kT}\right) \tag{21}$$

The large activation enthalphy of 5eV sets the upper limit for the ratio of the point defect concentration in thermal equilibrium to the atomic density of silicon to 10^{-6}, which eliminates the use of quenching experiments and absolute measurements as experimental techniques. At this point in time, no direct measurements of this kind exist for Si which would allow an unambigous interpretation. Progress in the understanding of Au diffusion in Si and oxidation-enhanced (OED) and -retarded (ORD) diffusion of group III and V dopants in Si, however, have shed new light at this twenty-five year old puzzle.

Accounting for both silicon self-interstitials and vacancies, Hu[43] has assumed that in thermal equilibrium, the diffusivity D^S of a substitutional dopant is the sum of components involving I and V contributions. The diffusion process via silicon self-interstitials is commonly called interstitialcy mechanism. Thus,

$$D_S = D_I^i \frac{C_I}{C_I^{eq}} + D_V^i \frac{C_V}{C_V^{eq}} \tag{22}$$

where D_I^i and D_V^i are the intrinsic diffusivities of the impurity atom, and C_x is the concentration of the corresponding point defect where superscripts denote equilibrium values.

Figure 8 shows values for the components of D^S calculated from experimental results[44]. Self-interstitials contribute more to diffusion for $T > 1000\,^{\circ}$C, and vacancies become dominant at lower temperatures.

Defining the fractional interstitialcy component

$$f_I = \frac{D_I^i}{D^i} \tag{23}$$

and point-defect supersaturation ratios (where x denotes either V or I)

$$S_x = \frac{C_x - C_x^{eq}}{C_x^{eq}} \tag{24}$$

Eq. (22) can be rewritten as

$$\frac{D}{D^i} = f_I \frac{C_I}{C_I^{eq}} + (1-f_I) \frac{C_V}{C_V^{eq}} \tag{25}$$

and the normalized diffusion enhancement, Δ_{ox} can be defined

$$\Delta_{ox} = \frac{D_{ox} - D}{D} = f_I S_I + (1-f_I) S_V \qquad (26)$$

where D_{ox} is the diffusivity under oxidation conditions. The effective diffusion coefficient in a specified oxidation time is obtained by time-averaging

$$<D> = \frac{1}{t} \int_0^t D \, dt \qquad (27)$$

The excess silicon self-interstitial concentration is related to the oxide growth rate via

$$C_I - C_I^{eq} = K' \left[\frac{dx}{dt} \right]^n \qquad (28)$$

where K' is a constant and $n = 0.3$ to 0.5. Inserting this equation and Eq. (26) into Eq. (27), the diffusivity can be calculated if the diffusion times and temperatures are given. Values for f_I can then be obtained by comparing Eq. (27) with experimental results for the diffusion coefficient obtained under oxidizing conditions.

For As, B and P, Matsumoto et al. [45] have performed this fitting experiment to the experimental results of Ishikawa et al. [46]. Figure 9 summarizes the temperature of f_I, which can be expressed as

$$f_{As} = 42 \exp \left[\frac{-0.542}{kT} \right] \qquad (29a)$$

$$f_B = 860 \exp \left[\frac{-0.829}{kT} \right] \qquad (29b)$$

$$f_P = 156 \exp \left[\frac{-0.666}{kT} \right] \qquad (29c)$$

Similar data have been presented by other authors [47]. For a comprehensive summary, I refer the reader to the review article by Tan and Gösele [44].

Contrary to As, B, and P, Sb exhibits a more complicated diffusion behavior. Figure 10 presents long time, high temperature results for Δ_{ox}. We notice that for these conditions, Sb has an ORD behavior. For short diffusion times, however, Sb data do not follow a constant f_I relationship, which indicates that C_V/C_V^{eq} has a strong influence on the diffusivity.

Antoniadis and Moskovitz [50,51] have investigated the time-dependence of the diffusivity. From their results in Fig. 11, it may be deduced that the diffusion of Sb in Si is dominated by a vacancy mechanism. Further results can be found in the original reference.

IV. Two-Dimensional Image Calculations for Optical Lithography

In projection printing, the image of the object — the mask — is projected onto the wafer through a high resolution optical lens, whose demagnification can vary between one to twenty times. The complete optical system is usually diffraction-limited.

The deviations from the ideal diffraction-limited system are measured by the mutual transfer function (MTF) of the lens. The MTF includes all aberrations such as spherical aberration, coma, astigmatism and field curvature. For a mask consisting of lines and spaces of spatial frequency ξ_p, the MTF is defined as the ratio of the mask modulation to the image modulation

$$\mathrm{MTF}(\xi_p) = \frac{\mathrm{M}_{\mathrm{Image}}(\xi_p)}{\mathrm{M}_{\mathrm{Mask}}(\xi_p)} \qquad (30a)$$

where

$$M_{Mask} = \frac{I_{max} - I_{min}}{I_{max} + I_{min}} \tag{30b}$$

and an equivalent expression for M_{Image}. The factors I_{max} and I_{min} are the maximum and minimum intensities, respectively. For an idealized optical system, the angle θ between the maximum diameter of the exit pupil and the image plane determines the resolution. This is described by the numerical aperture, NA, defined by

$$NA = n \sin \theta \tag{31}$$

or the effective f/number,

$$\frac{f}{\text{number}} = \frac{1}{2NA} \tag{32}$$

where n is the refractive index of the surrounding medium. The quality of the image depends critically on the illumination conditions. The illumination condition of most practical interest is partially coherent illumination. Partial coherence is quantified by the ratio

$$\sigma = \frac{NA_c}{NA_o} \tag{32}$$

where NA_c and NA_o are the numerical apertures of the condenser and objective lens, respectively. The parameter σ describes the degree of filling of the entrance pupil of the imaging lens by the source. It is the ratio of the imaged source at the entrance pupil to the pupil diameter. An incoherent source is a source of infinite dimension ($\sigma = \infty$), whereas a coherent source ($\sigma = 0$) is a point source. Over the last few years, the direct calculation of intensity distributions of lens images has advanced considerably.

Contrary to the near-field diffraction problems in the case of proximity printing, which have only been solved for a few simple cases, a rigorous theory is available to calculate the imaging properties of lenses for arbitrary objects. The basic theory of imaging with partially coherent light was developed by Hopkins [52] and Wolf [53] in the early 1950's. Several authors especially Kinzly [54], Watrasiewicz [55], Nyssonen [56], and Considine [57] simplified the original theory. Kintner [58], Offner [59] and Hershel [60] applied the theory to projection printing. Lacombat and Dubroeucq [61] and Tigreat [62] have studied step-and-repeat systems with partially coherent illumination. O'Toole and Neureuther [63] have incorporated the work of Kintner [58] into the program SAMPLE [64]. While one-dimensional calculations are relatively straightforward, the calculation of the image of an arbitrary two-dimensional mask is a tedious task. Griffing and Lorensen [65] have simulated two-dimensional geometries for incoherent illumination. To my knowledge, Lin's pioneering work [66] is still the only calculation for arbitrary masks with partially coherent illumination. He has studied non-periodic diffraction-limited images in and out of focus with different partially coherent illumination conditions. He has assumed circular pupils, non-reflective substrates, absorption-free photoresists and quasi-monochromatic illumination. His calculation starts from the mutual intensity distribution of illumination. Assuming a uniform circular source, the mutual intensity of the light incident on the object is given by [67]

$$J_{\bar{0}}\ (x_o - x_o', y_o - y_o') = \left(\frac{2J_1(\sigma)}{v} \right) I_{\bar{0}} \tag{33}$$

where x_o and y_o are coordinates in the object plane, J_1 is the Bessel function of the first kind of order one and

$$\nu = \frac{2\pi}{\lambda}\sqrt{(x_o'-x_o)^2 + (y_o'-y_o)^2}\, n_c \sin\theta_c \qquad (34)$$

The factor J_0^- is the intensity (assumed uniform) of the incident light, and $n_c \sin\theta_c$ is the numerical aperture of the condenser at the side of the imaging lens.

The factor I_o in Eq. (33) is taken to be one at the transparent part of the mask and zero at the opaque parts. The transfer function K is expressed by an integral and evaluated numerically. It is given by

$$K\,(x_o-x_o',y_o-y_o') = \frac{i}{\lambda^2}\int\int G\left\{\frac{\exp\,[ik(s-r)]}{sr}\right\} d\xi d\eta \qquad (35)$$

where $k = 2\pi/\lambda$, G is the aberration function of the imaging lens, r and s are the distances from the object and image points, $(x_o,y_o,0)$ and (x_o',y_o',z_o'), to the point (ξ,η,ζ) in the pupil plane of the imaging lens. In the absence of aberrations, G is set to one. Defocus is incorporated in s. The expression for K in Eq. (36) can be simplified using the paraxial approximation and integration

$$K(x_o-x_o',y_o-y_o') = \frac{n\sin\theta}{2\pi\lambda^2}\exp\left[\frac{i\nu}{(n\sin\theta)^2}\right]\int_0^1 J_0(u\rho)\exp\left\{-\frac{i\nu\rho^2}{2}\right\}\cdot\rho d\rho \qquad (36)$$

where $J_0(u\rho)$ is the Bessel function of the first kind of order zero, and $ns.5\theta$ is the numerical aperture of the imaging lens. The variables u and ν are normalized dimensionless coordinates for x and z of the form

$$u = \frac{2\pi}{\lambda}\, n\sin\theta\left[(x_o-x_o')^2 + (y_o-y_o')^2\right]^{\frac{1}{2}} \qquad (37)$$

$$\nu = \frac{2\pi}{\lambda}(n\sin\theta)^2 z \qquad (38)$$

The calculation of the diffraction image involves the solution of a four-dimensional integral. Several simplifications have been employed by Lin to reduce the amount of computation.

Figure 12a shows calculated diffraction images of a 1 μm × 1.2 μm contact hole and a 1 μm × 4 μm rectangular opening. An aberration-free lens with $NA = 0.32$ has been used for the calculations. The illumination is treated as monochromatic at $\lambda = 4047$Å. This figure compares the effect of illumination coherence on the image. The focal plane is specified by $z = 0$, which means that $z = 2\ \mu$m is equivalent to a 2 μm focus error from either side of the focal plane. Each contour in the figure is corresponds to a number which indicates the intensity level. There are a total of twenty levels ranging from 0,1,2, ..., 1,2, ..., to 9. Each level is 1.5 db from the next level. Comparing the case of an infinite σ (total incoherence) and $\sigma = 0$, the line edges of the image are less wavy but the image contrast is smaller. Furhermore, the total coherence case has a larger depth of focus.

Figure 12b compares calculated diffraction images for a lens with $NA = 0.32$ at $\lambda = 4047$Å to a lens with $NA = 0.16$ at $\lambda = 2200$Å. For both cases, the coherence factor is $\sigma = 0.78$. The result for the shorter wavelength and smaller aperture at a defocus of $z = 4\ \mu$m is similar to the other case at a defocus of $z = 2\ \mu$m, indicating that wavelength reduction is more preferable than a higher NA. This result has important implications for the further development of optical lithography.

V. Conclusions and the Future of Process Simulation

The past three years have brought significant progress in process simulation. In this paper, I have reviewed several new developments in ion implantation, diffusion and lithography. One of the important yet unresolved modeling problems remains the domain of two- (or even three-) dimensional oxidation on nonplanar surfaces. While first steps towards a more complete understanding of the oxidation process have been made [69-72], no model has been published yet which would allow a first-principles solution of oxidation phenomena on silicon substrates of arbitrary shape. Essentially all work has been restricted to the analysis of bird's beak geometries (e.g. [70,71]). It is without question, however, that local oxidation isolation schemes are not appropriate for scaled VLSI devices. Buried oxide isolation schemes offer many advantages to modern MOS processing. Apart from the obvious use as isolation structures between active device regions, trench isolation schemes are prime candidates for scaled CMOS technologies or DRAM storage elements.

Experimental studies of the oxidation of nonplanar silicon surface have been performed by Marcus and Sheng [73] as a function of temperature. Figure 13 shows TEM photographs of cross sections through oxidized silicon bars bounded by <100> and <110> planes. Oxidation was performed in wet O_2 at 900° (a), 950° (b), 1000° and 1100°C (d). The main results are the differences in oxide thickness for the different temperatures and plane orientations, the decreased oxide thickness at 950°C and 1050°C at the inner corner due to the reduced availability of oxidizing species, and the decreased oxide thickness at the upper corner due to the influence of local stress on the local solubility of oxygen in these regions. The effect of stress on oxidation kinetics is reduced for higher temperatures, confirming earlier results [69]. Similar results have been obtained for the oxidation of polysilicon gates [73].

The above result on twodimensional oxidation is just one example were further work is needed. Other examples would be the simulation of short time diffusion effects in rapid thermal annealing (RTA) experiments, better modeling of etching kinetics and deposition phenomena, and self-annealing phenomena in ion-implantation.

The development of future technologies will have to rely more and more on computer simulations in order to cut development costs. Major efforts will be necessary to make process simulation an equal partner to actual experiments. The following list contains several points which will have to be addressed in the near future:

Better understanding of basic processes

Complete process models

Better and faster numerical models

Improved user interfaces with enhanced graphics capabilities

Knowledge-based databases

Process simulation has a very bright future. The next few years will certainly bring solutions to most of the unresolved problem areas I have mentioned in this paper.

REFERENCES

[1] W. Fichtner, L. W. Nagel, B. R. Penumalli, W. P. Petersen and J. L. D'Arcy, *Proc. IEEE* **72**, 96 (1984).

[2] W. Fichtner, in *VLSI Technology*, (S. M. Sze, ed.), McGraw Hill 1983.

[3] R. W. Dutton, *IEEE Trans. ED*-**30**, 968 (1983).

[4] S. Furukawa and H. Ishiwara, in *Ion Implantation in Semiconductors*, (S. Namba, ed.), Plenum Press, New York 1975.

[5] W. S. Johnson and J. F. Gibbons, *Projected Range Statistics in Semiconductors*, Stanford University Bookstore 1969.

[6] S. Furukawa, H. Matsumura, and H. Ishiwara, *Jap. J. Appl. Phys.* **11**, 134 (1972).

[7] S. Mylroie and J. F. Gibbons, Proc. 3rd Intern. Conf. on Ion Implantation in Semiconductors and Other Materials, (B. L. Crowder, ed.) Plenum Press, New York, 1973, p. 243.

[8] P. Sigmund and J. B. Sanders, Proc. Intern. Conf. on Application of Ion Beams to Semiconductor Technology, Grenoble, (P. Glotin, ed.) 1967, p. 215.

[9] K. B. Winterbon, *Rad. Eff.* **13**, 215 (1972).

[10] D. H. Smith and J. F. Gibbons, in *Ion Implantation in Semiconductors 1976*, (F. Chernow, J. A. Borders and D. K.Brice, eds.) Plenum Press, New York 1977.

[11] L. A. Christel, J. F. Gibbons and S. Mylroie, *J. Appl. Phys.* **51**, 6176 (1980).

[12] L. A. Christel, J. F. Gibbons and S. Mylroie, *Nucl. Inst. Meth.* **182**, 187 (1981).

[13] M. D. Giles and J. F. Gibbons, *Nucl. Inst. Meth.* **209/210**, 33 (1983).

[14] D. K. Brice, *Appl. Phys. Letters*, **16**, 103 (1970).

[15] T. Tsurushima and H. Tanoue, *J. Phys. Soc. Japan*, **31**, 1695 (1971).

[16] S. Furukawa and H. Ishiwara, *J. Appl. Phys.*, **43**, 1268 (1972).

[17] J. P. Biersack and L. G. Haggmark, *Nucl. Inst. Meth.* **174**, 257 (1980).

[18] A. T. Macrander, Cornell University Report # 4234, April 1979.

[19] J. Lindhard, V. Nielssen and M. Scharff, *Mat. Fys. Medd. Dan. Vid. Selsk* **36**, 10 (1968).

[20] J. Lindhard, M. Scharff and H. E. Schiott, *Mat. Fys. Medd. Dar. Vid. Selsk* **33**, 14 (1963).

[21] J. Lindhard, V. Nielssen, M. Scharff and P. V. Thomsen, *Mat. Fys. Medd. Dan. Vid. Selsk* **33**, 18 (1963).

[22] O. S. Oen and M. T. Robinson, *J. Appl. Phys.* **35**, 2515 (1964).

[23] M. T. Robinson, *Marlowe-Binary Collision Cascade Simulation Program Version 11*, Oak Ridge National Laoratory, PSR-137, June 1978.

[24] T. Ishitani, R. Shimizu and K. Murata, *Jap. J. Appl. Phys.* **11**, 125 (1972); also Phys. Stat. Sol (b) **50**, 681 (1972).

[25] Y. Miyagawa and S. Miyagawa, *J. Appl. Phys.* **54**, 7124 (1983).

[26] W. P. Petersen, W. Fichtner and E. H. Grosse, *IEEE Trans. ED-* **30**, 1011 (1983),; also to be published.

[27] I. Adesida and L. Karapiperis, *Rad. Eff.* **61**, 223 (1982).

[28] J. Gibbons, W. S. Johnson and S. Mylroie, *Projected Range Statistics*, 2nd edition, John Wiley and Sons, NY 1975.

[29] D. K. Brice, *Ion Implantation Range and Energy Deposition Distributions*, IFI/Plenum New York 1975.

[30] W. K. Hofker, D. P. Oesthoek, N. J. Koeman and H. A. M. de Grefte, *Rad. Eff.* **24**, 223 (1975).

[31] H. Ryssel, H. Kranz, K. Muller, R. A. Henkelmann and J. Biersack, *Appl. Phys. Lett.* **30**, 399 (1977).

[32] S. Kalbitzer and H. Oetzmann, *Rad. Eff.* **47**, 57 (1980).

[33] K. Winterbon, P. Sigmund and J. B. Sanders, *Mat. Fys. Medd. Dan. Vid. Selsk.* **37**, 14 (1970).

[34] A. M. Mazzone and G. Rocca, *IEEE Trans. CAD*-**3**, 64 (1984).

[35] A. de Salvo and R. Rosa, *Rad. Eff.* **47**, 117 (1980).

[36] M. Kendall and A. Stuart, *The Advanced Theory of Statistics — Volume I — Distribution Theory*, Macmillan Publishing Co., New York 1977.

[37] K. B. Winterbon, *Appl. Phys. Lett.* **42**, 205 (1983).

[38] S. E. Hansen, *SUPREM-III USER's GUIDE*, Stanford 1983.

[39] B. R. Penumalli, *IEEE Trans. ED*-**30**, 986 (1983).

[40] H. Ryssel, K. Haberger, K. Hoffmann, G. Prinke, R, Dumcke and A. Sachs, *IEEE Trans. ED*-**27**, 1484 (1980).

[41] R. B. Fair, in *Impurity Doping Processes in Silicon*, (F. F. Y. Wang, ed.) North Holland, New York, 1981, pp. 315-441.

[42] A. Seeger and K. P. Chick, *Phys. Stat. Sol.* **29**, 455 (1968).

[43] S. M. Hu, *J. Appl. Phys.* **45**, 1567 (1974).

[44] U. Gösele and T. Y. Tan, in *Defects in Semiconductors*, (J. Narayan and T. Y. Tan, eds.) North Holland 1981.

[45] S. Matsumoto, Y. Ishikawa and T. Nishi, *J. Appl. Phys.* **54**, 5049 (1983).

[46] Y. Ishikawa, Y. Sakina, H. Tanaka, S. Matsumoto and T. Nishi, *J. Electrochem. Soc.* **129**, 644 (1982).

[47] T. Y. Tan, U. Gösele and F. F. Morehead, *Appl. Phys. A***31**, 97 (1983).

[48] S. Mizuo and H. Higuchi, *Jap. J. Appl. Phys.* **20**, 739 (1981).

[49] T. Y. Tan and B. J. Ginsberg, *Appl. Phys. Lett.* **42**, 448 (1983).

[50] D. A. Antoniadis and I. Moskovitz, in *Aggregation Phenomena of Point Defects in Silicon*, (E. Sirtl and J. Goorissen, eds.), The Electrochemical Society 1983, p.1.

[51] D. A. Antoniadis and I. Moskovitz, *J. Appl. Phys.* **53**, 6788 (1982).

[52] H. H. Hopkins, *Proc. Roy. Soc. (London)*, **A208**, 263 (1951); see also *Proc. Roy. Soc. (London)*, **A217**, 408 (1953); *Proc. Roy. Soc. (London), B* **69**, 562 (1956); *J. Opt. Soc. Am.* **47**, 508 (1957).

[53] E. Wolf, *Proc. Roy. Soc. (London)*, **A225**, 96 (1954); see also *Proc. Roy. Soc. (London)*, **A230**, 246 (1955).

[54] R. E. Kinzly, *J. Opt. Soc. Am.*, **55**, 1002 (1965); see also *J. Opt. Soc. Am.* **46**, 9 (1956).

[55] B. M. Watrasiewicz, *Optica Acta* **12**, 391 (1965).

[56] D. Nyssonen, *Appl. Opt.* **16**, 2223 (1977).

[57] P. S. Considine, *J. Opt. Soc. Am.* **56**, 1001 (1966).

[58] E. C. Kintner, *Appl. Opt.* **17**, 2747 (1978).

[59] A. Offner and J. Meiron, *Appl. Opt.* **8**, 183 (1969).

[60] R. Hershel, *Kodak Microelectronics Seminar Proceedings Interface 178, 62 (1978); see also SPIE* **135** Developments in Semiconductor Microlithography III, 24 (1978).

[61] M. Lacombat and G. M. Dubroeucq, SPIE **174**, Developments in Semiconductor Microlithography VI, 28 (1979).

[62] P. Tigreat, SPIE **174**, Developments in Semiconductor Microlithography IV, 37 (1979).

[63] M. M. O'Toole and A. R. Neureuther, SPIE **174**, Developments in Semiconductor Microlithography IV, 22 (1979).

[64] SAMPLE User's Guide, Electronics Research Laboratory, Dept. of Electrical Engineering and Computer Science, UC Berkeley, Berkeley, 1982.

[65] B. F. Griffing and W. E. Lorensen, 1983 IEEE *Symposium on VLSI Technology*, Digest of Technical Papers, p. 76.

[66] B. J. Lin, IEEE Trans. ED-**27**, 931 (1980).

[67] M. Born and E. Wolf, *Principles of Optics*, Pergamon Press, New York 1959.

[68] B. J. Lin, in *Proceedings of the International Conference on Microlithography – Microcircuit Engineering 81*, compiled by A. Oosenbrug, September 28-30, 1981, Lausanne, Switzerland, p. 47.

[69] E. P. Eernisse, *Appl. Phys. Lett.* **30**, 290 (1977).

[70] D. Chin, R. W. Dutton, S. Y. Oh, J. L. Moll and S. M. Hu, 1982 *International Electron Devices Meeting*, Digest of Technical Papers, p. 228.

[71] H. Matsumoto and M. Fukuma, 1983 *International Electron Device Meeting*, Digest of Technical Papers, p. 39.

[72] G. Charitat and A. Martinez, *J. Appl. Phys.* **55**, 909 (1984).

[73] R. B. Marcus and T. T. Sheng, *J. Electrochem. Soc.* **129**, 1278 (1982).

Table I - IC Process Steps		
Thermal Processing and Doping	Pattern Definition	Pattern Transfer
Epitaxy Ion Implantation Predeposition Annealing Drive-In Oxidation	Optical Lithography Electron Beam Lithography Ion Beam Lithography X-Ray Lithography	Wet Chemical Etching Ion Milling Reactive Ion Etching CVD Evaporation Sputtering

Table II

Classification of Theories

Method			Range					Damage	Reference
			R_p	ΔR_p	$\gamma,\beta...$	ΔK	Multi-layer		
Transport Theory		1st order	o	x	x	x	x	x	[5]
		2nd order	o	o	x	o	x	x	[6]
		3rd order	o	o	o	Δ	x	x	[7]
	Integral Equation		o	o	o	o	x	o	[8-10]
			o	o	o	o	o	o	[11-13]
Inter-mediate Methods	Two Step Method		o	o	x	Δ	Δ	o	[14,15]
	Semi-Monte-Carlo Method		o	o	x	x	o	o	[16]
Monte Carlo			o	o	o	o	o	o	[17,18]

o; calculated, Δ; possible, x; impossible or inaccurate

Table III

Pearson Distributions for Ion Ranges*
Type I (incomplete β-function of 1st kind)
$f(x) = k(x-x_-)^{m_1}(x_+-x)^{m_2}$, $x_\pm = \frac{-b \mp \sqrt{d}}{2b_2}$, $m_{1,2} = \frac{1}{2b_2} \mp \frac{b_1(1+2b_2)}{2b_2\sqrt{d}}$, $(x_- \leqslant x \leqslant x_+,\ m_1>0,\ m_2>0)$
Type III (incomplete Γ-function)
$f(x) = k \exp\left(\frac{-x}{b_1}\right)(x_+-x)^m$, $x_+ = -b_0/b_1$, $m = 1 + b_0/b_1^2$, $(b_1<0,\ -\infty \leqslant x \leqslant x_+,\ x_+>0,\ m>0)$
Type IV
$f(x) = k\,\lvert b_0+b_1x+b_2x^2\rvert^{\frac{1}{2b_2}} \exp\left\{- \frac{\frac{b_1}{b_2}+2b_1}{\sqrt{-d}} \tan^{-1}\left[\frac{2b_2x+b_1}{\sqrt{-d}}\right]\right\}$ $(d < 0,\ \frac{1}{2b_2} < -5/2,\ -\infty \leqslant x \leqslant +\infty)$
Type VI (incomplete β-function of 2nd kind)
$f(x) = k(x_--x)^{m_1}(x_+-x)^{m_2}$, $x_\pm = \frac{-b_1 \pm \sqrt{d}}{2b_2}$, $m_{1,2} = \frac{1}{2b_2} \mp \frac{b_1(1+2b_2)}{2b_2\sqrt{d}}$, $(-\infty \leqslant x \leqslant x_- < x_+,\ m_1>0,\ m_1+m_2 < -1)$

* k = normalization constant, $d = b_1^2 - 4b_0b_2$

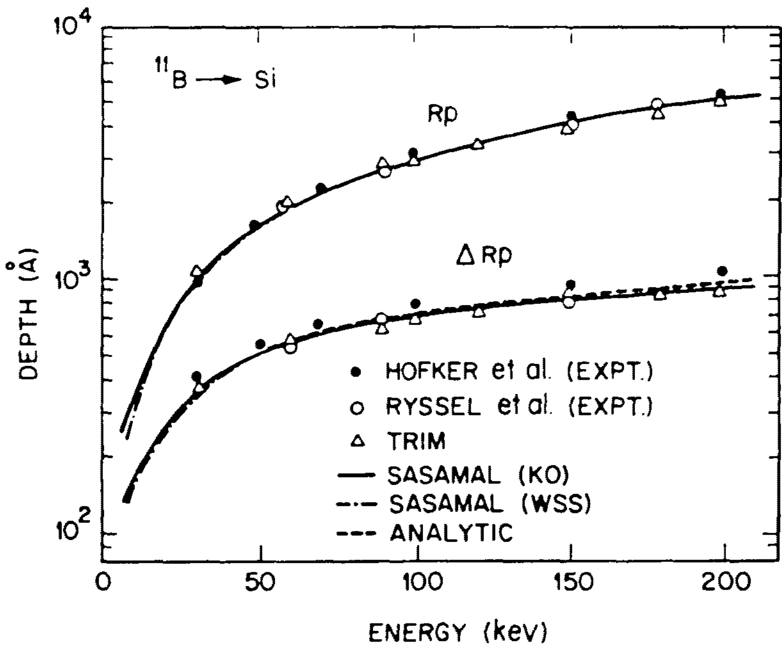

Fig. 1 Mean projected rande R_p and standard deviation ΔR_p for 5 - 200 keV ^{11}B implanted into amorphous Si. SASAMAL [25] with Kalbitzer- Oetzmann [32] cross section (solid curve) and WSS cross section [33] calculations are compared with experimantal results by Hofker et al. [30] (closed circles) and Ryssel et al. [31] (open circles) and with TRIM calculations [17]. The analytical results of Gibbons et al. [28] and Brice [29] are identical and represented by the dashed line. (From Miyagawa and Miyagawa [25]).

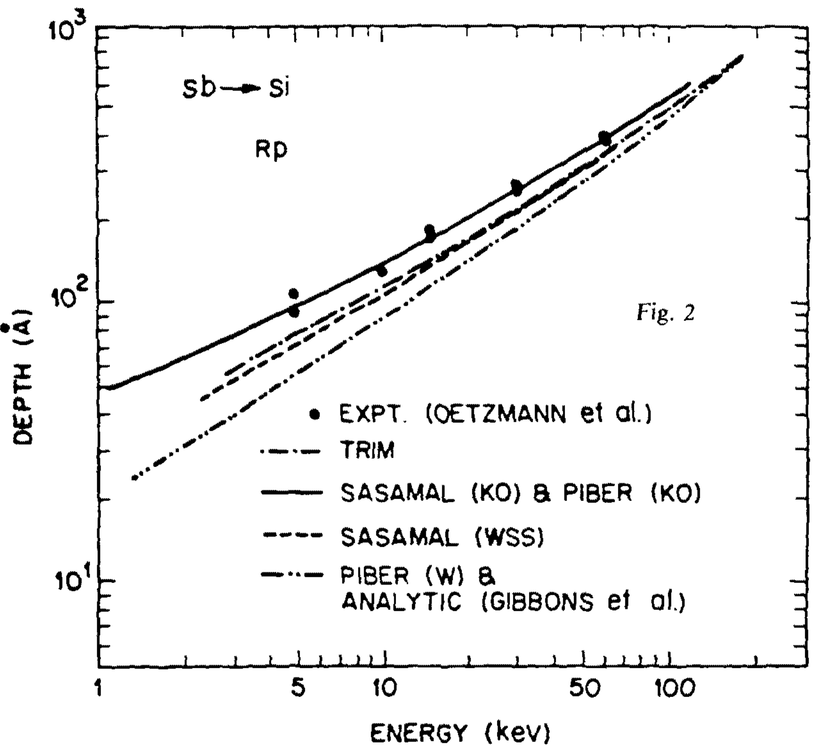

Fig. 2

Mean projected range R_p for ^{122}Sb implanted into amorphous Si. SASAMAL (with two cross sections [25]) and PIBER (with two cross sections [25]) are compared to experiments [32] and analytical results [28]. (From Miyagawa and Miyagawa [25]).

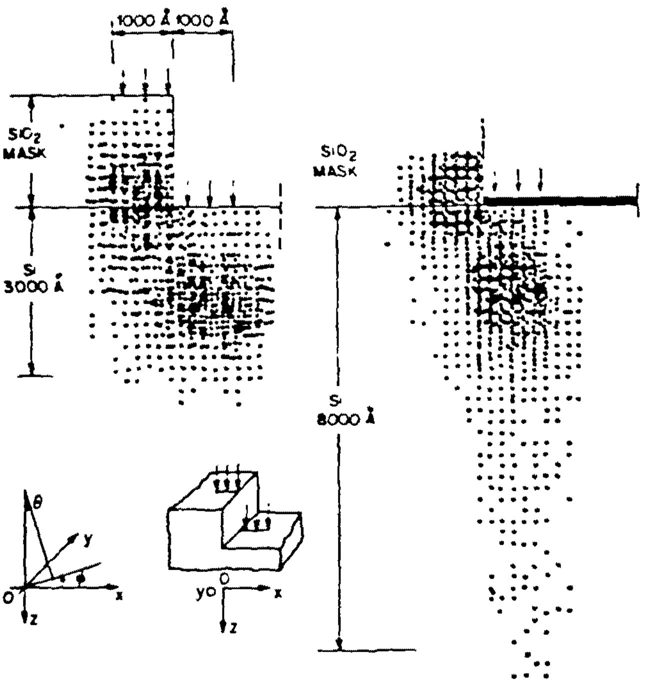

Fig. 3 Fig. 4

^{31}P implant into a partially masked by 2000A SiO_2. Also shown are coordinate axes and angles. (From Mazzone and Rocca [34]).

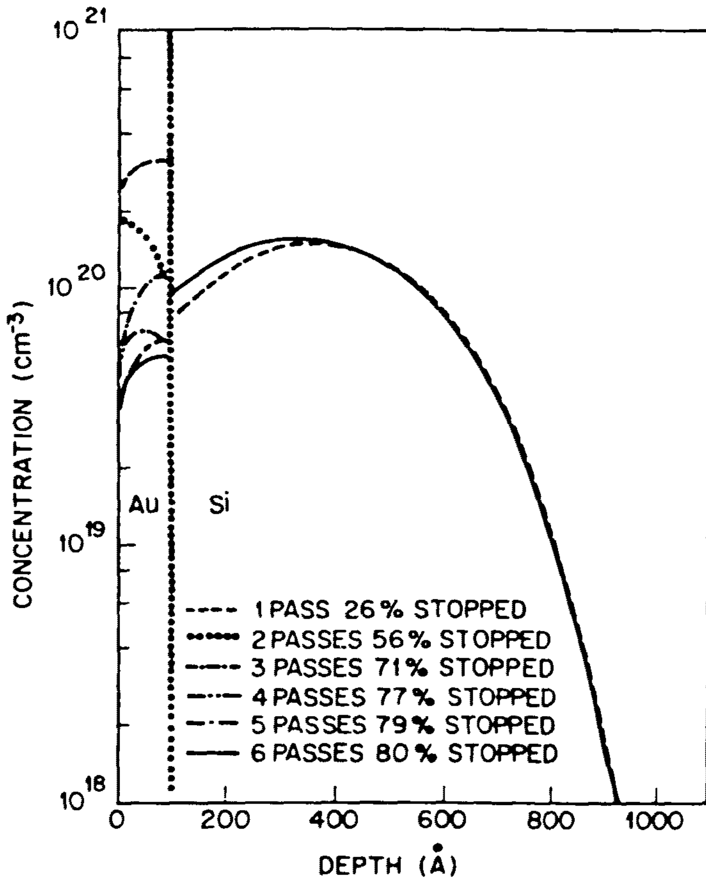

Fig. 5 Implanted profile for a ^{11}B implant (15 keV, 10^{15}cm^{-2} into 100Å of Au on Si at a dose of 10^{15}cm^{-2} (From Giles and Gibbons [13]).

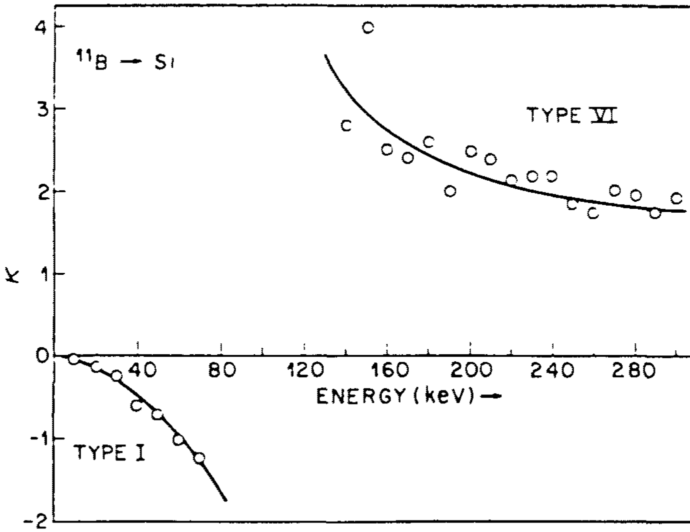

Fig. 6 $\kappa = b_1^2/4b_0b_2$ as a function of energy for ^{11}B → Si (From Petersen et al. [26]).

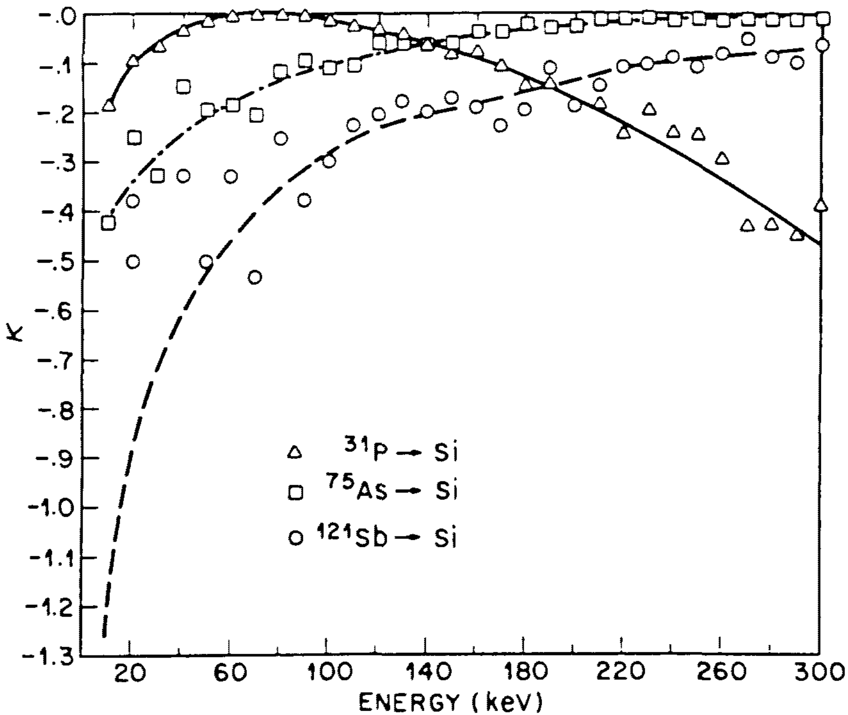

Fig. 7 $\kappa = b_1^2/4b_0b_2$ as a function of energy for ^{31}P, ^{75}As and ^{122}Sb. (From Petersen et al. [26]).

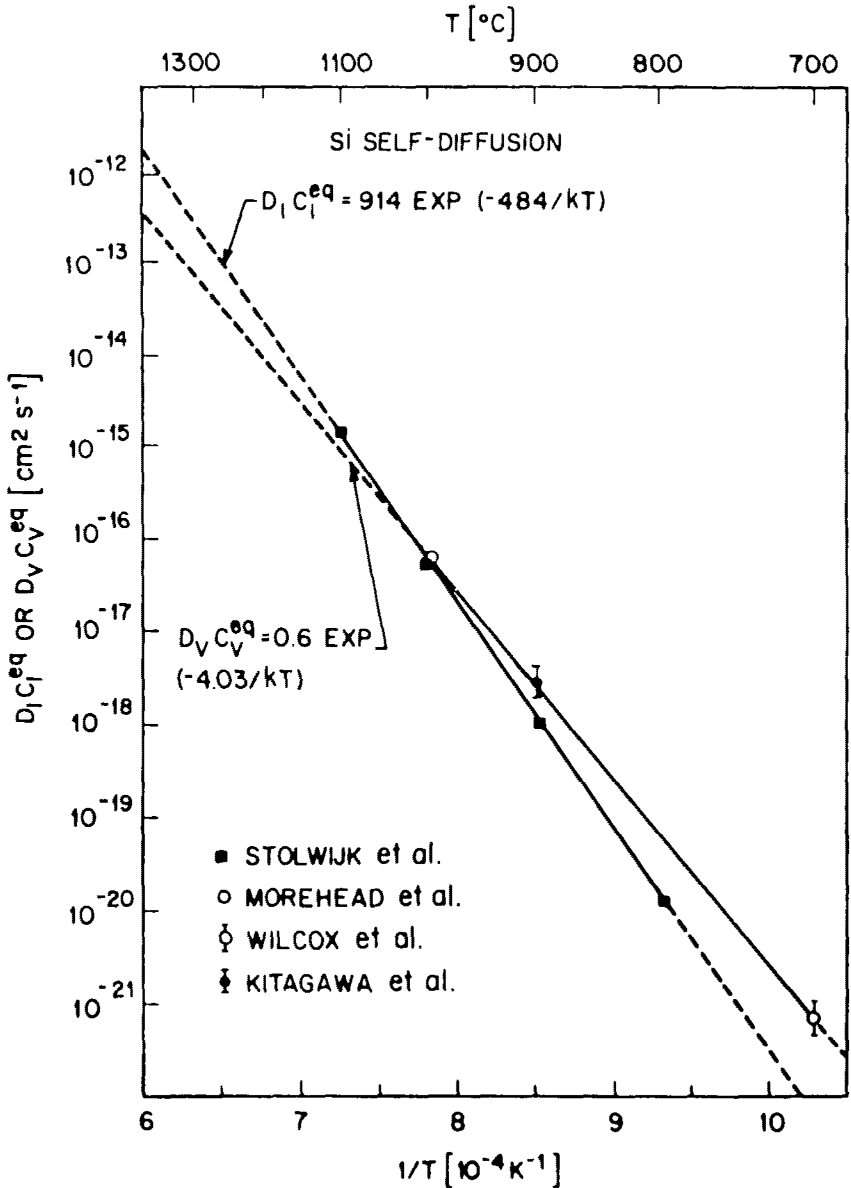

Fig. 8 Components $D_I C_I^{eq}$ and $D_V C_V^{eq}$ of Si self-diffusion versus $1/T$ calculated from the diffusion of Au into dislocation-free Si and $D_V C_V^{eq}$ calculated from the diffusion and precipitation of Ni in dislocated Si. (From Gösele and Tan [44]).

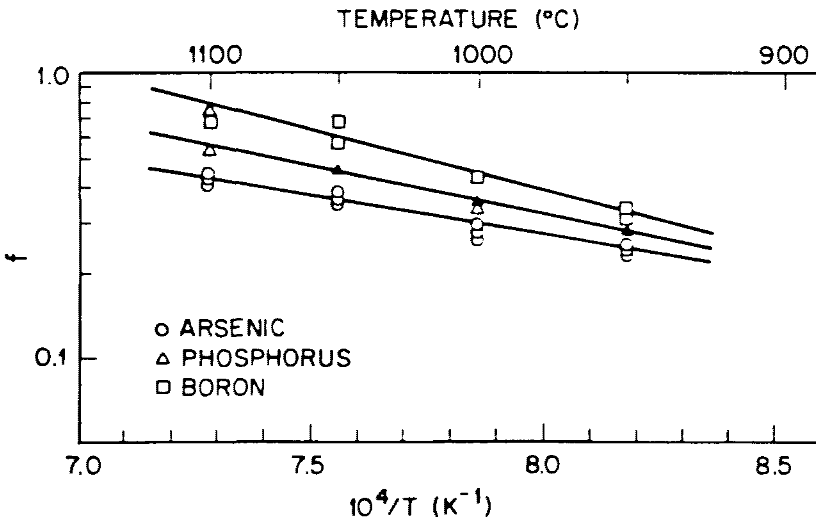

Fig. 9 Temperature dependence of the fraction od interstitialcy diffusion of As, B, and P in Si. (From Matsumoto et al. [45]).

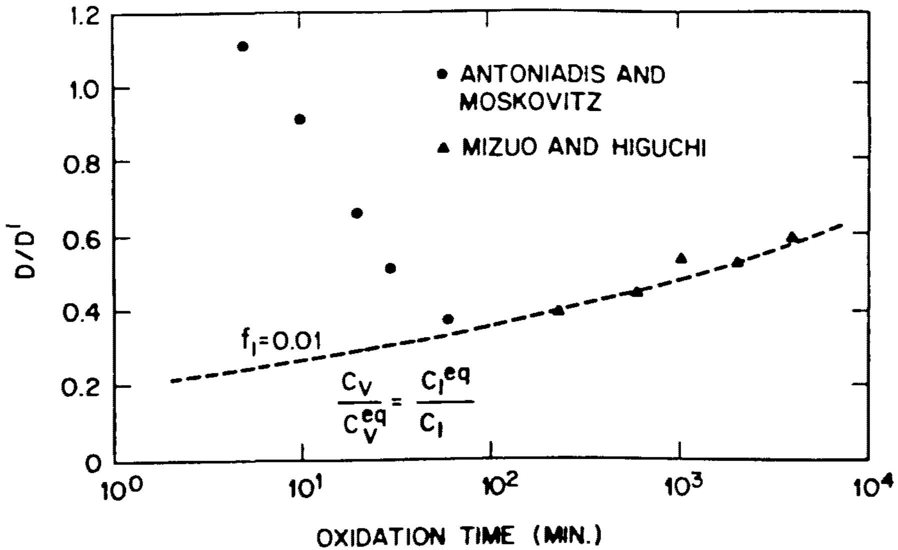

Fig. 10 Fit of available Sb ORD data. (From Tan et al. [47])

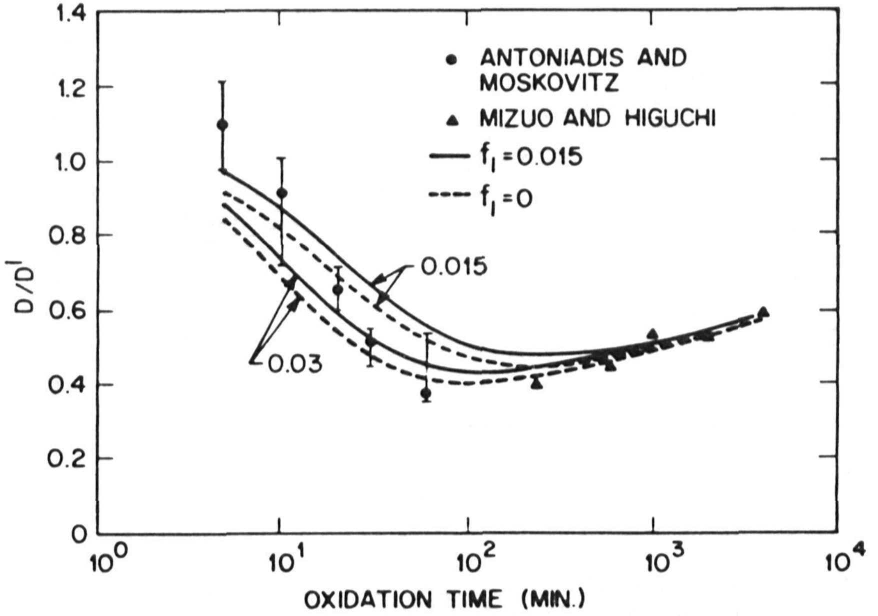

Fig. 11 Calculations of normalized Sb diffusivity during oxidation for $f_I = 0.01$ and $C_V/C_V^{eq} = C_I/C_I^{eq}$. (From Antoniadis and Moskovitz [48]).

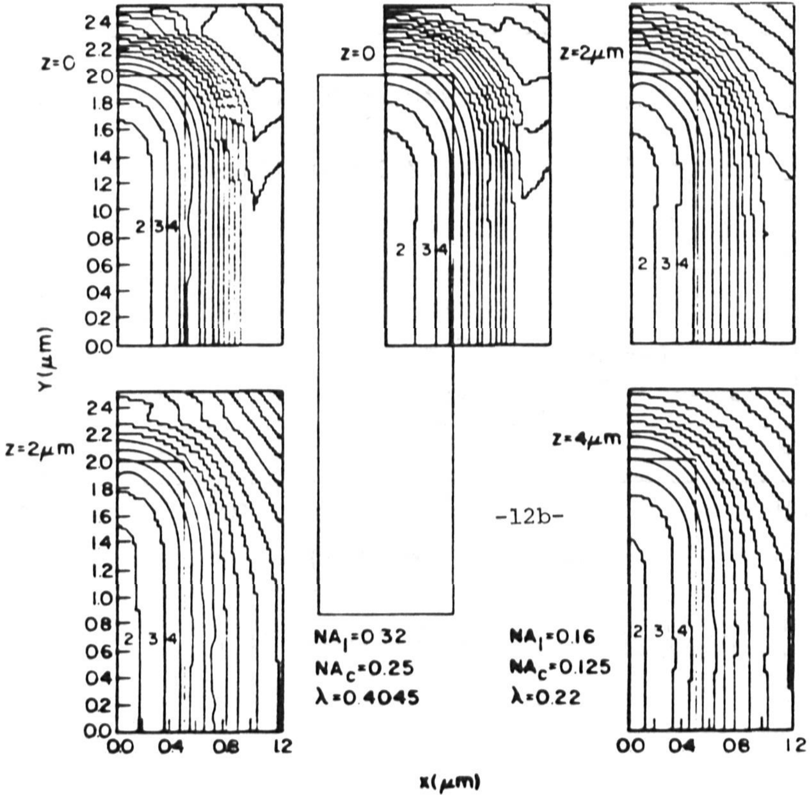

-12b-

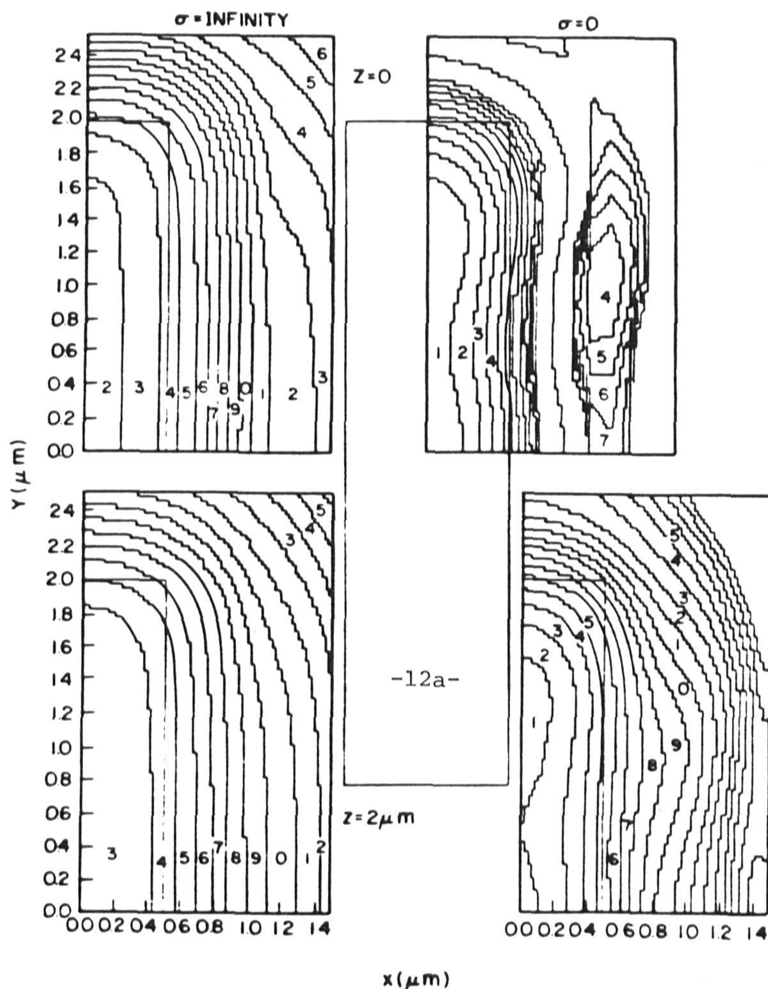

Fig. 12 Diffraction image for $NA = 0.32$, $\lambda = 4045\text{Å}$ at $\sigma = 0$ and $\sigma = \infty$. The parameter z indicates the distance from the focal plane. (a) Image in focus ($z = 0$) and out of focus ($z = 2\ \mu m$) of a $1\ \mu m \times 1.2\ \mu m$ contact hole and a $1\ \mu m \times 4\ \mu m$ rectangular opening. (b) Image of two parallel rectangular openings of uneven lengths, for $NA = 0.32$ at $\lambda = 4045\text{Å}$ and $NA = 0.16$ at $\lambda = 2200\text{Å}$. (From Lin [66]).

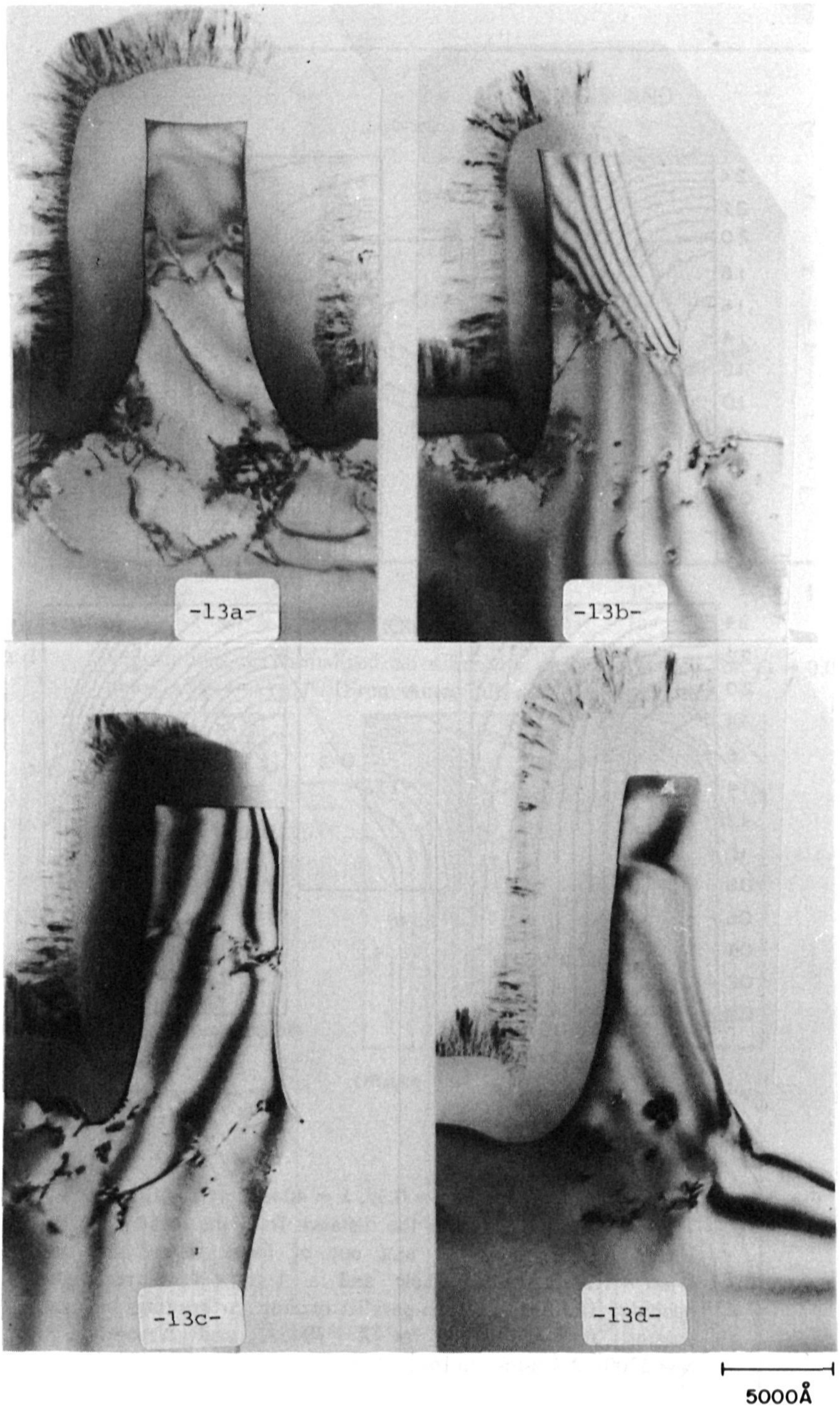

Fig. 13 Transmission electron Micrographs of cross sections of silicon samples oxidized in wet O_2 at (a) 900°C, (b) 950°C, (c) 1000°C, and (d) 1100°C. (From Marcus and Sheng [73]).